Ultramicroscopy 111 (2011) 1599–1606

Contents lists available at SciVerse ScienceDirect

Ultramicroscopy

journal homepage: www.elsevier.com/locate/ultramic

# Are electron tweezers possible?

Vladimir P. Oleshko [a,*], James M. Howe [b]

[a] National Institute of Standards and Technology, Gaithersburg, MD 20899, USA
[b] Department of Materials Science and Engineering, University of Virginia, Charlottesville, VA 22904-4745, USA

ARTICLE INFO

*Article history:*
Received 11 February 2011
Received in revised form
20 August 2011
Accepted 25 August 2011
Available online 6 September 2011

*Keywords:*
Electron tweezers
Manipulation
Nanoparticles
Metal alloys
Plasmons
VEELS
EFTEM

ABSTRACT

Positively answering the question in the title, we demonstrate in this work single electron beam trapping and steering of 20–300 nm solid Al nanoparticles generated inside opaque submicron-sized molten Al–Si eutectic alloy spheres. Imaging of solid nanoparticles and liquid alloy in real time was performed using energy filtering in an analytical transmission electron microscope (TEM). Energy-filtering TEM combined with valence electron energy-loss spectroscopy enabled us to investigate *in situ* nanoscale transformations of the internal structure, temperature dependence of plasmon losses, and local electronic and optical properties under melting and crystallization of individual binary alloy particles. For particles below 20 nm in size, enhanced vibrations of the dynamic solid–liquid interface due to instabilities near the critical threshold were observed just before melting. The obtained results indicate that focused electron beams can act as a tool for manipulation of metal nanoparticles by transferring linear and angular mechanical momenta. Such thermally assisted electron tweezers can be utilized for touchless manipulation and processing of individual nano-objects and potentially for fabrication of assembled nanodevices with atomic level sensitivity and lateral resolution provided by modern electron optical systems. This is by three orders of magnitude better than for light microscopy utilized in conventional optical tweezers. New research directions and potential applications of trapping and tracking of nano-objects by focused electron beams are outlined.

© 2011 Elsevier B.V. All rights reserved.

## 1. Introduction

Understanding physical principles for controlling the dynamic behavior of nanoparticles in inhomogeneous gas (liquid)–solid systems is becoming increasingly important for nano-scale science and technology. Nondestructive trapping and manipulation of small particles in a liquid using a laser beam, which is refracted by the particle and transfers momentum to it, is known as a single-beam gradient force optical trap, or optical tweezers [1–3]. Optical tweezers have become a highly developed and heavily used tool of choice for many applications in biology, physics and chemistry, when gentle and remotely controllable manipulation of micro- and nano-objects is required. Nowadays, electromagnetic forces in optical tweezers are often employed to trap dielectric and metal particles ranging in size from tens of nanometers to several micrometers, and to manipulate them in all spatial directions [4–6]. Furthermore, 3D-trapping and orientation of individual Au nanorods using plasmon resonance has been performed [7] and holographic tweezers have been developed to trap tailored arrays of multiple micron-size objects [8,9]. The implementation of optical tweezers at a surface offers exciting opportunities for the elaboration of future lab-on-a-chip devices entirely operated with light. The transition from conventional 3D tweezers to 2D is made possible by exploiting evanescent fields bound at interfaces. In particular, stable trapping of single dielectric beads using surface plasmons (SP) under non-focused illumination has been recently demonstrated [10], whereas fine tuning of nanoparticle positions has been theoretically evaluated to be realizable by coupling to plasmonic nanostructures [11].

Our previous experiments utilizing partially molten submicron-sized Al–Si alloy spheres and a focused electron beam in a medium-voltage transmission electron microscope (TEM) [12–15] and numerical calculations of linear and angular momentum transfer from an electron beam to small particles in a scanning TEM (STEM) by others [16,17] indicate that optical trapping of particles by focused electron beams may occur. Although an experimental set-up is challenging, since it requires the trapping of particles in vacuum, TEM appears indeed as a promising technique to study optically trapped particles, providing an excellent spatial resolution (currently down to 48 pm) [18] when sub-nanometer electron beams are employed. Analytical electron microscopy (AEM) expands further potentialities of TEM for studying structural transformations of nanoscale materials by adding analytical capabilities such as energy-filtering imaging (EFTEM), electron energy-loss spectroscopy (EELS) and energy-

* Corresponding author. Tel.: +1 301 975 5970.
*E-mail address:* vladimir.oleshko@nist.gov (V.P. Oleshko).

0304-3991/$ - see front matter © 2011 Elsevier B.V. All rights reserved.
doi:10.1016/j.ultramic.2011.08.015

dispersive X-ray spectrometry (EDXS), which allow one to probe local electronic and optical response properties, and more recently other physical (mechanical, transport) properties of nanostructured materials (see Ref. [19]). *In situ* AEM allows one to combine (S)TEM imaging and spectroscopy at up to sub-eV energy resolution with physical and chemical processing (e.g., heating/cooling, radiation damage experiments, and gas (vapor)–solid chemical reactions in environmental cells). These capabilities transform such instruments into a versatile micro- and nano-lab for high-spatial resolution analyses of various dynamic processes and fabrication of new materials and devices [14,15,20,21]. In this work, we demonstrate single electron-beam trapping and steering of solid nanoparticles inside individual opaque submicron-sized molten Al–Si eutectic alloy spheres during melting and crystallization of Al–Si eutectic alloy particles by EFTEM and valence EELS (VEELS). For this purpose, we employ the focused electron beam as a multifunctional probe for providing the following means in the course of experiments:

(a) fine temperature tuning during generation of solid Al nanoparticles inside submicron-sized molten Al–Si eutectic alloy spheres;
(b) monitoring nanoscale transformations of the internal structure, local electronic and optical properties under melting and crystallization of individual binary eutectic alloy particles, including plasmon imaging of solid metal particles inside opaque molten Al–Si alloy particles in real time;
(c) trapping, steering and re-melting of the Al nanoparticles.

## 2. Materials and methods

Atomized powder of Al-11.6 at% Si alloy, which has a eutectic (initial melting) temperature of 577° C and a liquidus (final melting) temperature of 581° C [22], was placed in a test tube of ethanol and dispersed using an ultrasonic cleaner. The test tube was removed from the cleaner and the larger particles were allowed to settle in the test tube for at least 1 h. The smaller particles (20–400 nm in diameter) present in the topmost liquid were collected in an eyedropper and deposited onto ultrathin carbon films supported by Cu-mesh grids. The 20–400 nm diameter particles of Al-11.6 at% Si alloy were examined in a JEOL[1] 2010 F Schottky field-emission analytical electron microscope. The instrument was equipped with a Gatan Model 678 Imaging Filter operated at 197 kV. EEL spectra were recorded at the energy resolution of 1.0 eV, based on the measured full-width at half-maximum of the zero-loss peak. Video recording of EFTEM images was carried out using a VCR with a time resolution of 1/30 s. Each frame was then imported into a Macintosh G4 computer with a video capture board and Adobe Premier 5.0 software. The particles were heated in the microscope using a Gatan double-tilt ($\pm 30^\circ$) heating holder with a maximum obtainable temperature of 800 °C. Real-time plasmon imaging of melting/crystallization of Al nanospheres inside the submicron-sized Al–Si alloy particles was performed with a 6–10 eV energy window centered at the first Al plasmon peak at 15 eV.

## 3. Results and discussions

In the following sections, we first discuss melting of the Al-11.6 at% Si alloy particles and observation of the changes that occur inside the particles during this process using EFTEM. We then examine the effect of the melting transition on the EEL spectra and optical properties of the nanoparticles. Understanding these behaviors is important for interpretation of the ability to use the electron beam as an "electron tweezer" to steer a solid Al nanoparticle inside molten Al–Si alloy liquid. This process is then demonstrated experimentally and followed by an analytical analysis, which explains the gradient force necessary for such a process to occur. Lastly, further potential possibilities of using such electron tweezers are described.

### 3.1. EFTEM/VEELS of melting of Al–Si alloy particles

In this part, we discuss an investigation of the melting of the Al-11.6 at% Si eutectic alloy submicron and nano-sized particles *in situ*. When the temperature was increased just below the liquidus of 581° C [22], the particles partially melted to form a stable two-phase solid–liquid mixture, consisting mainly of a spherical-shaped solid α-Al nanoparticle inside a spherical shell of liquid Al–Si alloy, all of which is contained inside the submicron-sized particles by a thin aluminum-oxide shell on the particle surface [12,23]. Zero-loss filtering often improves the contrast and resolution of the particle structures as compared to conventional TEM imaging because blurring and chromatic aberration due to inelastically scattered electrons are eliminated. However, internal structural details for the particle shown in the zero-loss (elastic electron) image (Fig. 1, $0 \pm 5$ eV) are hardly visible due to its thickness of 223 nm. Contrast tuning using energy filtering at selected energy losses provided better phase separation of the Al-rich areas from 10 to 20 nm-sized Si-rich precipitates using the Al volume plasmon (VP) losses ($15 \pm 5$ eV) and allowed identification of the non-uniform oxide shell 5–15 nm thick at oxide plasmon losses ($25 \pm 5$ eV) (Fig. 1). The oxide shell contains the Al-rich liquid in the particle when it is partially or fully molten and undergoes creep to relieve the high stress on the order of 15 GPa

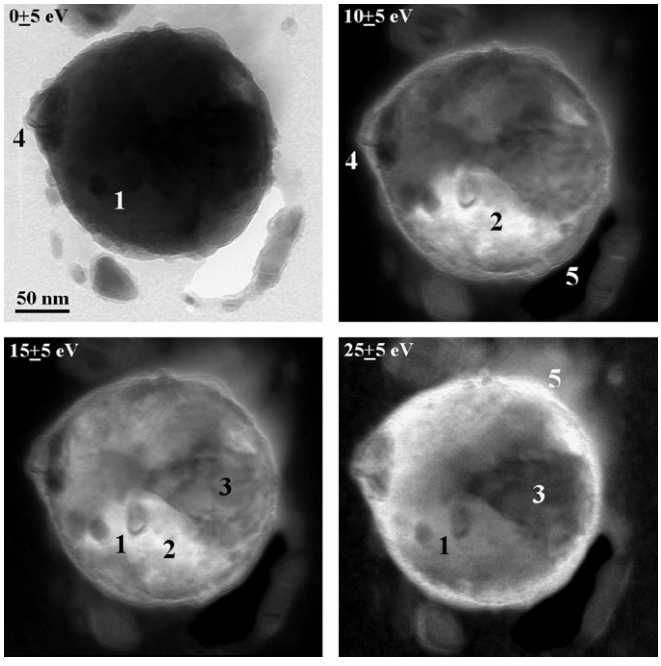


**Fig. 1.** A molten Al-11.6 at% Si particle at $T=656$ °C. EFTEM, a 10 eV window centered at 0, 10, 15 and 25 eV energy losses. Contrast tuning under energy filtering in the range between 0 and 25 eV reveals structural details of a molten single-crystal α-Al matrix with multiple embedded 10–20 nm Si precipitates (1), α-Al-rich area (2), Si-rich area (3), defect cavern (4), as a result of ejection of liquid through a 5–15 nm-thick oxide shell containing the alloy (5), and its rupture during melting.

[1] Certain commercial equipment, instruments, or materials are identified in this document. Such identification does not imply recommendation or endorsement by the National Institute of Standards and Technology, nor does it imply that the products identified are necessarily the best available for the purpose.

generated by the 10.4% volume change of expanding liquid [23]. *In situ* plasmon imaging revealed a small fraction of the particles with aluminum oxide shells containing preexisting critical defects, which were ruptured by through-thickness cracking during melting. Some of the pressurized liquid alloy inside the particle is ejected through a crack due to the internal pressure produced by the tangential stress in the shell that was even able to damage a supporting carbon film touching the particle. Real-time observations of structural features inside the partially molten particles using contrast tuning are discussed in Section 3.2.

EEL spectra with contributions both from the Al–Si alloy particle and two (top and bottom) thin oxide layers, demonstrate the shift of the first VP from 15.2 eV at 25 °C, when the entire particle is solid, to 14.7 eV at 623 °C, when it is liquid, as well as corresponding shifts of three higher order plasmon peaks (Fig. 2a). The energy of VP resonance given by the Langmuir frequency is

$$E_p = \hbar\omega_p^f = \hbar[ne^2/(\varepsilon_0 m)]^{0.5}, \quad (1)$$

where $n$ is the electron density, $e$ is the electron charge, $\varepsilon_0$ is the permittivity of vacuum, and $m$ is the electron mass. Above room temperature the free electron plasma frequency, $\omega_p^f$ depends on the electron density as a linear function of temperature [24]

$$\hbar\omega_p^f = E_{po} - B\Delta T, \quad (2)$$

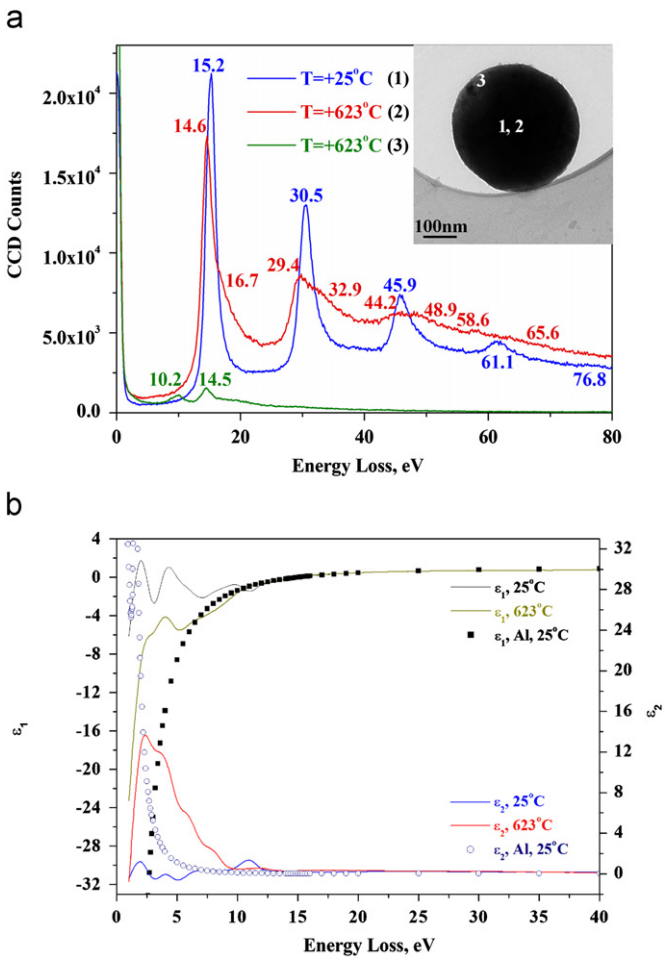


**Fig. 2.** (a) *In situ* EEL spectra recorded at the center (1,2) and at the edge (3) of an Al–Si alloy particle (left inset) at 25 °C (1) and at 623 °C (2, 3), respectively. (b) The effective complex dielectric permittivity, $\varepsilon = \varepsilon_1 + i\varepsilon_2$ derived from spectra 1 and 2 using Kramers–Kronig relations and reference points (filled squares and open circles from [27]).

where $E_{po}$ is the plasmon energy at given temperature, $B$ is the slope (for Al, $B = 3/2\beta E_{po} = 5.8 \pm 0.7 \times 10^{-4}$ eV/degree), $\beta$ is the linear expansion coefficient, and $\Delta T$ is the change in the temperature. The energy of the VP resonance at $T = 623$ °C estimated according to Eq. (2) is 14.9 eV. It is fairly close to the experimental value of 14.7 eV, indicating that the temperature dependence of the VP energy in the molten sphere is dominated by plasmon losses in the liquid Al. The right-side shoulders are due to the enhanced contribution from Si-rich precipitates. Similar shifts in the first VP peak have been observed for wetting of a Si surface by molten Al [25]. Spectra 1 and 2 in Fig. 2a exhibit drastic changes in the shapes and symmetries of the peaks with temperature. The EEL spectrum recorded *in situ* at 623 °C near the particle edge (spectrum 3) also displays a weak peak at 10.2 eV, assigned to SP multipole modes with $E_p/\sqrt{2} = 10.3$ eV [14]. A Fourier-log deconvolution was employed to remove plural scattering effects. Coherent plural scattering contributions for the second and third plasmons were removed after smoothing the related spectral regions. The single scattering EEL intensity expressed as the differential cross-section $d^2\sigma/d\Omega dE$ is related to the imaginary part of the reciprocal complex dielectric permittivity $\varepsilon(q, E)$ as a function of wave vector $q$ and energy $E$. It thus reflects the local dielectric response of the media to a longitudinal field:

$$d^2\sigma/d\Omega dE \propto \mathrm{Im}[-1/\varepsilon(q,E)]\ln(1+\beta^2/\theta_E^2), \quad (3)$$

where $\beta$ is the collection semi-angle (the illumination semi-angle $\alpha < \beta < (E/E_0)^{0.5}$), $\theta_E = E/2T/\sqrt{1-\beta^2}$. the characteristic scattering angle, $\beta = v/c$; $T = 0.5 m_e v^2 = E_0(1+E_0/2m_e c^2)/(1+E_0/2m_e c^2)^2$; $m_e$ is the free electron mass; $v$ is the velocity of the incident electrons; $c$ is the velocity of light, and $E_0$ is the initial energy of the incident electrons. It was shown that a semiclassical dielectric function-based formalism gives the same results in terms of description of EELS as a quantum-mechanical theory if all the inelastic signal is collected [26].

A Kramers–Kronig dispersion analysis was employed to calculate the energy dependence of the dielectric permittivity. Since the energy-loss function $\mathrm{Im}[-1/\varepsilon(\boldsymbol{q}, E)]$ is usually overwhelmed by a zero-loss peak, the Kramers–Kronig analysis appears to be sensitive to variations of the single scattering intensities at the low-energy side. This could introduce uncertainties at energy losses below 3 eV. In order to overcome this problem, a smooth extrapolation of the single scattering intensities to zero energy was applied. The Kramers–Kronig analysis of the spectra showed substantial changes in dielectric parameters with temperature (see Fig. 2b), including the appearance of a composite absorption band in $\varepsilon_2$ between 1 and 9 eV, displaying local maxima at 2.3, 3.6, 5.7 and 7.7 eV. Meanwhile, at 25 °C, the dielectric constants appear to be in agreement with reported reflectance measurement data for polycrystalline Al films at energy losses $E > 11$ eV [27]. Weak oscillations in absorption $\varepsilon_2$ and in polarization $\varepsilon_1$ below 11 eV could perhaps be assigned to interband transitions at about 2.0 eV and 4.0 eV. Further considerations for interpretation of the low-loss features should take into account effects of inhomogeneity in the alloy particle on the band structure and metal-induced gap states possible at Al/Si interfaces and in Si-rich precipitates as well as the presence of an oxide shell and coupling to surface plasmons (a feature at 10.9 eV).

The Kramers–Kronig derived complex refractive index, (Fig. 3a) is defined as

$$N = \varepsilon^{1/2} = n + ik, \quad (4)$$

where refraction, $n = \sqrt{0.5(\sqrt{\varepsilon_1^2+\varepsilon_2^2}+\varepsilon_1)}$, and extinction, $k = \sqrt{0.5(\sqrt{\varepsilon_1^2+\varepsilon_2^2}-\varepsilon_1)}$. The curves for $n(E)$ and $k(E)$ (and also the

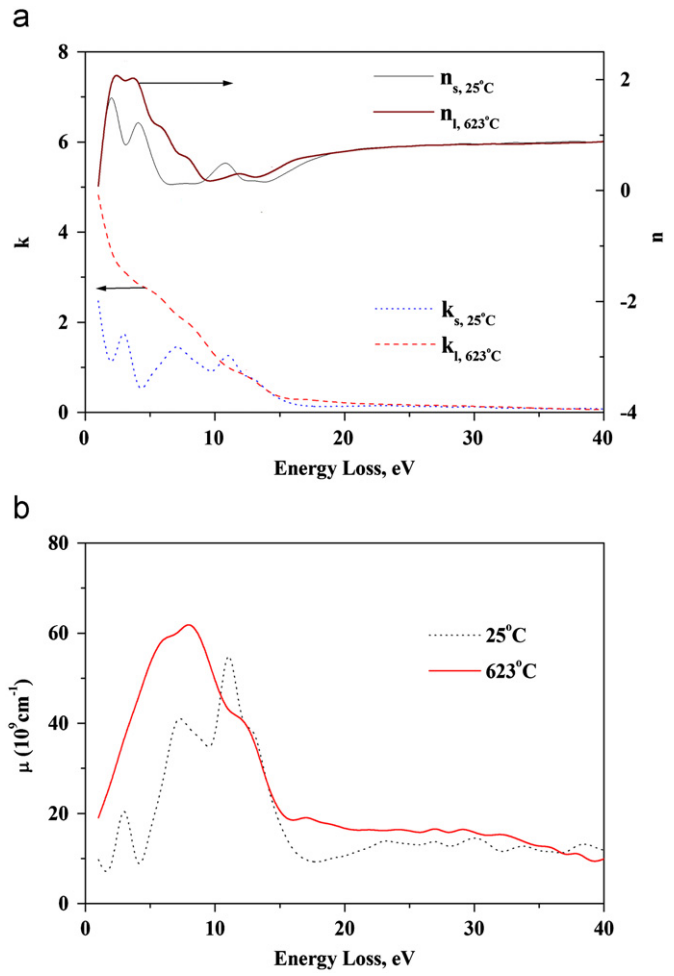


**Fig. 3.** (a) Complex refractive index, $N=\varepsilon^{1/2}=n+ik$, and (b) absorption coefficient, $\mu=2Ek/\hbar c$ for solid ($T=+25$ °C) and molten ($T=+623$ °C) Al–Si alloy particle, respectively, derived via Kramers–Kronig transformations.

curves for $\varepsilon_1$ and $\varepsilon_2$) cross each other if superimposed on the same scale at roughly 15 eV, the plasmon energy. For the liquid particle, similarly to the dielectric permittivity, the refractive index displays a substantial enhancement in both refraction and extinction below 20 eV energy loss as compared to the solid particle. The absorption coefficient, $\mu=2Ek/\hbar c$, shown for comparison in Fig. 3b, revealed a low-energy shift and broadening of absorption bands between 3 and 20 eV energy losses. Dielectric and optical properties reflect both (a) typical metallic properties of liquid aluminum with the conduction-electron absorption that appears to follow a free-electron Drude model and wide range of modifications in the interband spectrum [27], and (b) nanoscale inhomogeneities due to Si-rich precipitates and to a minor extent of the 5–15 nm-thick protective oxide shell. In the liquid state, aluminum exhibits no interband structure because there is no long-range order and no well-defined band structure or Brillouin-zone boundaries. Expected differences in refraction between solid and molten phases at elevated temperatures that likely contribute to a backwards trapping force will be discussed in the Section 3.2. Summarizing, *in situ* EFTEM/VEELS study indicates that melting above the liquidus in individual Al-11.6 at% Si alloy submicron-sized particles is accompanied by nanometer scale transformations of the internal eutectic structures that in turn induce significant changes in local electronic and optical properties, particularly in the liquid alloy.

### 3.2. *Thermally-assisted single electron-beam trapping and steering of crystalline Al nanospheres*

Thermally assisted motion of crystalline Al nanospheres confined within the partially molten Al–Si particles was initiated by the electron beam, which was used to control and to observe the trapping in real time (Fig. 4). At 577–581 °C, the alloy particles are partially molten and form a solid–liquid two-phase mixture [12]. Contrast tuning using energy filtering at 15–25 eV energy losses was employed to observe structural features inside the partially molten particles ("ball-in-ball" plasmon imaging) and to provide better distinction between solid and liquid phases. Real-time video observations show that 20–300 nm diameter Al-rich solid nanospheres can be generated, trapped, steered and melted inside the submicron-sized molten binary alloy particles using temperature control and a focused electron beam (Fig. 4). Thickness fringes indicate that the 40 nm diameter nanosphere inside the heated alloy particle is still crystalline. The crystalline Al nanosphere followed a focused electron beam as it was translated and/or tilted. The particle also followed the beam when the stage was moved in lateral directions under a stationary beam (Fig. 4b and c). Typically metal nanoparticles could be easily transferred across distances of 40–100 nm limited by available

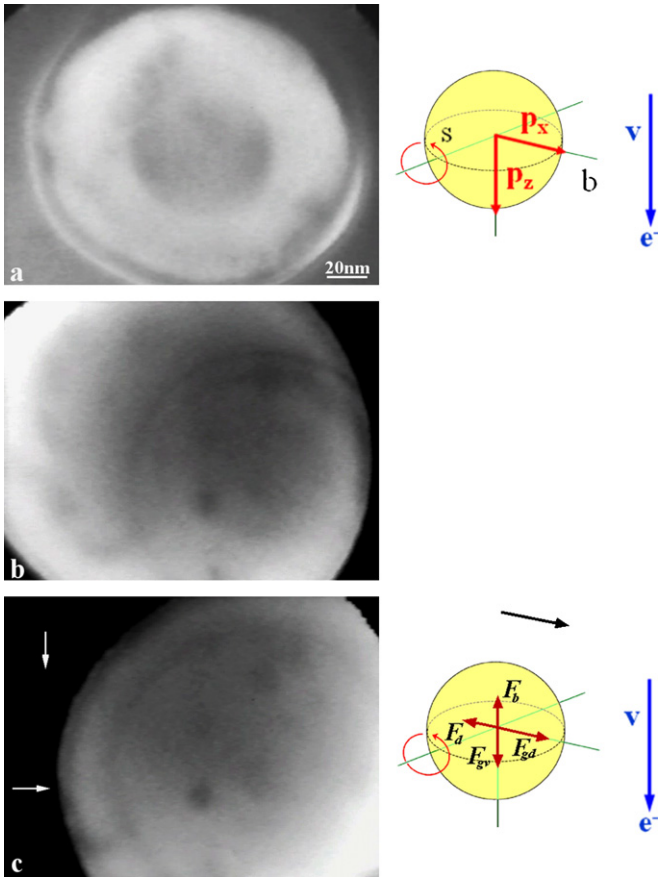


**Fig. 4.** *In situ* EFTEM, 15 eV energy loss, a 6 eV window. (a) Electron beam-assisted generation of a 70 nm-diameter solid particle inside a partially molten Al-11.6 at% Si sphere surrounded by a 10 nm thick oxide shell. (b, c) Steering of a solid particle by translating the beam and/or moving the microscope stage in directions shown by arrows. The video frame (b) is separated from the frame (c) by 17 s. The upper inset in (a) describes transfer of a momentum $\boldsymbol{p}=(p_x, p_z)$ of a fast electron with impact parameter $b$ and velocity $v$ to a polarizable particle via electromagnetic interaction [16]. Here $S$ is a surface embedding the particle. The bottom inset in (c) schematically describes forces exerted on the trapped particle. $\boldsymbol{F}_{gv}$, $\boldsymbol{F}_d$, $\boldsymbol{F}_b$ and $\boldsymbol{F}_{gd}$ denote gravitational, drag, buoyant and gradient forces, respectively. The black arrow indicates the direction of the translation of the beam.

internal volume of the molten sphere at speed of about 20–40 nm/s in chosen directions using the beam shift, tilting and/or shifting the microscope stage. In the course of irregular antipersistant fractional Brownian motion, the nanosphere generally should have a tendency to return to the center in the bottom of the partially molten particle because the density of solid Al ($\rho_s=2.55\times10^3$ kg/m$^3$) at the melting point is greater than that of liquid Al ($\rho_l=2.39\times10^3$ kg/m$^3$) or liquid Al–Si alloy [12]. We found that solid nanospheres could be sequentially generated, manipulated and re-melted inside the neighboring molten alloy particles (Fig. 5). Notably, for particles below 20 nm in size, plasmon imaging at 1/30 s time resolution revealed enhanced vibrations of the dynamic solid–liquid interface due to instabilities near the critical threshold just before melting.

The observed behavior evidently indicates that there is an attractive force between the electron probe and Al nanosphere. According to [1,16], a frequency-dependent refraction (Fig. 3a), contributes to a backward gradient force in single-beam gradient force traps, which should overcome scattering and gravitational forces. The latter causes the nanosphere to sink or move towards the bottom of the molten particle, as well as the scattering force of the electrons, which constantly act to push the particle away from the electron beam. As a result, the solid Al nanosphere acts as a weak positive lens, allowing it to be manipulated by an electron beam in a TEM. The origin of the attractive force between the electron beam and Al nanosphere is likely similar to optical trapping of dielectric spheres in liquids [1–3]. In conventional trapping, when a laser beam is focused on the solid sphere, momentum transfer to the particle occurs due to refraction of the macroscopic emerging radiation. Since the complex refractive index and density of the solid crystalline nanosphere is slightly higher than the refractive index of the liquid alloy, the sphere acts as a weak positive lens. Assuming that it represents the system with multiple resonant frequencies and interacting dipoles that are affected by local fields, the relative refraction, $N_s/N_l$ of solid and molten phases at elevated temperatures contribute to a backwards trapping force via the complex particle polarizability [28,29],

$$\alpha=3/N[(N_s/N_l)^2-1/(N_s/N_l)^2+2] \quad (5)$$

Here $N$ is the number of oscillating dipoles in the trapped particle and the real and imaginary parts of the refractive index, $N_{s,l}=\varepsilon_{s,l}^{1/2}$, are linked through the Kramers–Kronig relations because of causality involved in system's response. The resulting forces on the particle due to refraction of electrons lead to a net backwards trapping force that is sufficient to steer the Al nanosphere in the liquid alloy. It seems unlikely that the electron beam transfers momentum to the metallic Al nanosphere just by the excitation of plasmons. Due to limitations imposed by the cut-off plasmon wavevector, collective oscillations are heavily damped above its critical value, $q_c\sim E_p/\hbar v_f$ . In this case, the phase velocity of the plasma oscillations $E_p/q$ equals the Fermi velocity $v_f$ and all the energy is transferred to an excited single electron of the Fermi sea followed by dissipation of the energy through interband transitions [30].

Considering elastic collisions between the incident electrons and/or Al atoms in the liquid alloy and a spherical crystalline particle of the mass, $M$, the maximum momentum transferred to the particle, $P$, can be estimated as

$$P=\sqrt{2MT_{max}} \quad (6)$$

Here, $T_{max}=2E(E+2mc^2)/Mc^2$ is the maximum energy transferable to the solid particle from an incident electron [31], where $E=m_ec^2(1/\sqrt{1-\beta^2}-1$ and $m_e$ is the electron mass. Similarly, for elastic collision of an Al atom in the liquid with the particle, the maximum transferable energy, $T_{max}=4m_{\mathrm{Al}}ME/(m_{\mathrm{Al}}+M)^2$, where the kinetic energy, $E=MV^2/2$, $V=\sqrt{3RT/1000A}$ is the speed of the Al atom, $m_{\mathrm{Al}}$ is the mass of an Al atom, $R$ is the universal gas constant, $T$ is the temperature of the liquid Al–Si, and $A$ is the atomic mass of Al. The calculated momentum of the particles for electron and Al atom collisions at $T=580$ °C is larger than the one for the particles measured experimentally from their average speed (see Table 1). This means that both the incident electrons and liquid atoms have the potential to provide sufficient energy transfer to initiate a motion of the solid nanoparticles in the liquid. Similar calculations are performed for a two-step process, whereby an electron collides first with an Al atom and the Al atom subsequently impacts the solid nanosphere, give the maximum momentum transferred of $1.61\times10^{-21}$ Ns [12], which is also sufficient to move the particles. In addition to elastic collisions, one should consider another kind of interaction of the incident electrons with the metallic nanosphere, e.g., refraction, which is typically associated with conventional optical trapping [1,2,6,16]. The momentum transferred by a single refracted electron at an accelerating voltage of $U=200$ kV is, $p=\hbar k=h/\lambda=F\Delta t\approx2.64\times10^{-22}$ Ns at electron wavelength $\lambda=2.51$ pm. Here $F$ is the force that the electron exerts for a time period $\Delta t$. Although the momentum transferred by a single electron is very small, the number of electrons incident on the nanosphere per unit time is enormous (1 to $2\times10^{10}$ electrons/s$^{-1}$ per projected area of the nanosphere), so the total transferred momentum due to refraction of electrons would exert a force on a particle of $F=2.6$ to $5.3\times10^{-12}$ N. This force is of the same order of

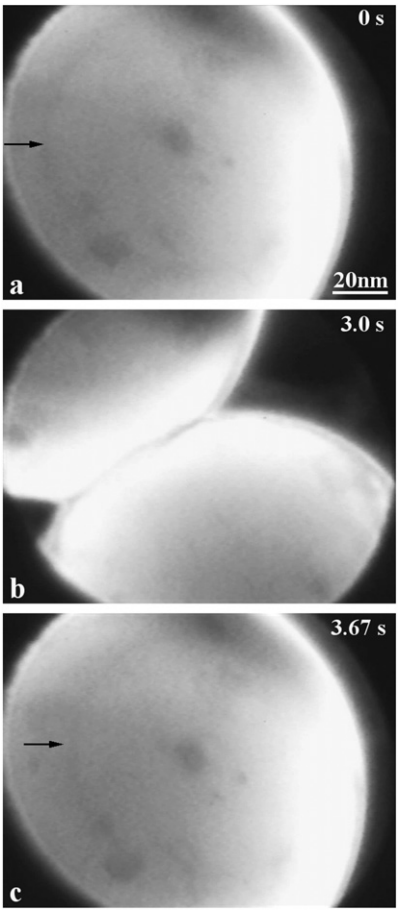


**Fig. 5.** EFTEM video frames at 15 eV energy loss, a 6 eV window, showing sequential generation of solid nanoparticles inside neighboring partially molten submicron Al–Si alloy spheres after 0.0 s (a), 3.0 s (b) and 3.67 s (c). The arrows indicate the edges of barely visible solid particles.

**Table 1**
The experimentally measured momentum and forces exerted on solid nanoparticles of various sizes in liquid Al–Si alloy in comparison with the calculated momentum for electron and Al atom collisions

| Radius (nm) | Mass (kg) | Speed (nm/s) | Momentum (Ns) | Force (N) | | |
|---|---|---|---|---|---|---|
| | | | | Drag | Gravitation | Buoyant |
| 73 | $4.16\times10^{-18}$ | 15.4 | $6.41\times10^{-26}$ | $2.79\times10^{-17}$ | $4.07\times10^{-17}$ | $3.82\times10^{-17}$ |
| 37 | $0.54\times10^{-18}$ | 7.7 | $4.16\times10^{-27}$ | $7.06\times10^{-18}$ | $5.30\times10^{-18}$ | $4.97\times10^{-18}$ |
| Electron | $9.11\times10^{-31}$ | – | $5.28\times10^{-22}$ ($r$=73 nm) $5.28\times10^{-20}$ ($r$=37 nm) | – | – | – |
| Al atom in liquid Al–Si $T$=580 °C | $4.48\times10^{-26}$ | – | $7.20\times10^{-22}$ ($r$=73 nm) $8.21\times10^{-23}$ ($r$=37 nm) | – | – | – |

magnitude as those forces that drive small particles during typical optical laser beam trapping [11].

The motion of the solid nanosphere in a liquid alloy is influenced by several driving forces [12,13,16], including drag, $\boldsymbol{F}_d$, gravitational, $\boldsymbol{F}_{gv}$, buoyant, $\boldsymbol{F}_b$, radiation, $\boldsymbol{F}_r$, and gradient, $\boldsymbol{F}_{gd}$, forces as schematically shown in the inset, Fig.4c. So, the total force exerted on a particle is

$$\boldsymbol{F}=\boldsymbol{F}_d+\boldsymbol{F}_{gv}+\boldsymbol{F}_b+\boldsymbol{F}_r+\boldsymbol{F}_{gd} \tag{7}$$

The drag or fluid resistance force, $F_d=6\pi\eta r v\rho_l$, exerted on the solid spherical nanoparticle by the liquid under the lamellar motion conditions at very low values of the Reynolds number, $R_e=\mathrm{vr}/\eta$ ($R_e=2.4\times10^{-7}$ [12]) is of the order of 0.7 to $2.8\times10^{-17}$ N. Here, $\eta$ is the kinematic viscosity (for liquid Al at melting point, $\eta=5.50\times10^{-7}$ m$^2$/s); $r$ is the particle radius, $v$ is its average speed (nm/s) obtained from video recording and $\rho_s$ is the density of solid Al ($\rho_{sAl}=2.55$ g/cm$^3$ at the melting point). The gravitation force, $F_{gv}=\rho_s V_s g$, is of the order of 0.5 to $4\times10^{-17}$ N, where $V_s$ is the particle volume, $g=9.8$ m/s is the free fall acceleration. The buoyant force, $F_b=\rho_l V_s g$, is of order of 0.5 to $3.8\times10^{-17}$ N, where $\rho_l$ is the density of liquid Al (for liquid Al, $\rho_l=2.39$ g/cm$^3$). According to [16], the radiation force acting on the nanoparticle due to radiation emitted as a result of interaction with the electron is negligibly small. Comparison of the magnitudes of various forces exerted on the solid nanospheres (Table 1) shows that, similar to conventional optical trapping [6], the electromagnetic gradient force induced by fast refracted electrons should dominate over all other forces to make stable particle trapping possible. This force is given by the integral of Maxwell's stress tensor over a surface $S$ embedding the particle [29]. For $F\approx F_{gd}$, this yields the total momentum transferred to the particle

$$\mathbf{P}=\int_{-\infty}^{\infty}\frac{d\boldsymbol{P}}{d\omega}d\omega=\int_{-\infty}^{\infty}\boldsymbol{F}_{gd}(\omega)\delta(\omega)d(\omega)=\boldsymbol{F}_{gd}(\omega=0), \tag{8}$$

where $d\boldsymbol{P}/d\omega=1/\pi\oint_s\mathbf{T}(\boldsymbol{r},\omega=0)\,d\boldsymbol{s}$ is the Fourier transform of the zero-frequency component of Maxwell's stress tensor

$$\mathbf{T}(r,w=0)\int_{-\infty}^{\infty}[\varepsilon_0\boldsymbol{E}(r,\omega)\boldsymbol{E}^*(r,\omega)-\varepsilon_0/2\mathbf{I}\mathbf{E}(r,\omega)\boldsymbol{E}(r,\omega)\boldsymbol{E}*(r,\omega)+\mu_0\mathbf{H}(r,\omega)\mathbf{H}^*(r,\omega)-\mu_0/2\mathbf{I}\mathbf{H}(r,\omega)\mathbf{H}^*(r,\omega)]dt,$$

in dyadic form over frequency expressed in terms of the Fourier transforms of the external electric $\mathbf{E}(\boldsymbol{r},\omega)$ and magnetic $\mathbf{H}(\boldsymbol{r},\omega)$ fields (see Eqn. 2 in [16] and Eqn. 6 in [17]).

In addition to the gradient force, a passing electron induces a torque on the solid nanosphere making it rotate in a liquid alloy by changing its angular momentum (Fig. 6). For a small isotropic particle far away from the electron beam as schematically shown in (Fig. 4, inset), the force exerted by each frequency component of the external field $\boldsymbol{E}^{ext}(\boldsymbol{r},\omega)$ can be described using the expressions for the electric and magnetic fields induced by the polarizable particle in terms of its frequency-dependent polarizability $\alpha$ (Eqn. 3 in [16]). In the $\omega\to0$ limit, $F_{gdz}(\omega)=0$ but $F_{gradx}$ goes to a finite value, which depends on the real part of the polarizability

$$\mathrm{F}_{gdx}(\omega=0)\sim\mathrm{Re}\{\alpha(0)\}/\mathrm{v}^2b^3 \tag{9}$$

Numerical integration yields the transferred momentum for large impact parameter $b$ and long wavelengths (Fig. 4, top inset), assuming that the particle is described by its polarizability (refraction, Eqn. 6 in [16]). The momentum transfer from a fast electron to a small particle and ultimately to a single atom can be described [16] using the classical dynamic polarizability of the atom as input, provided the atom does not intersect the atom, i.e., it moves in a region in which the atomic orbitals have already decayed sufficiently. The frequency-resolved momentum transfer can directly give the probability for the electron to transfer a given amount of momentum, while losing a given quantum of energy ($\hbar v$), so the distribution of momentum transfers from the electron to a single atom can be calculated in this way from classical theory, and should agree with a quantum electrodynamics formulation of the problem. The only difference between a single atom and a large particle is that the latter will accumulate many scattering events without significant recoil between them, and thus, it can directly give access to the noted average [32].

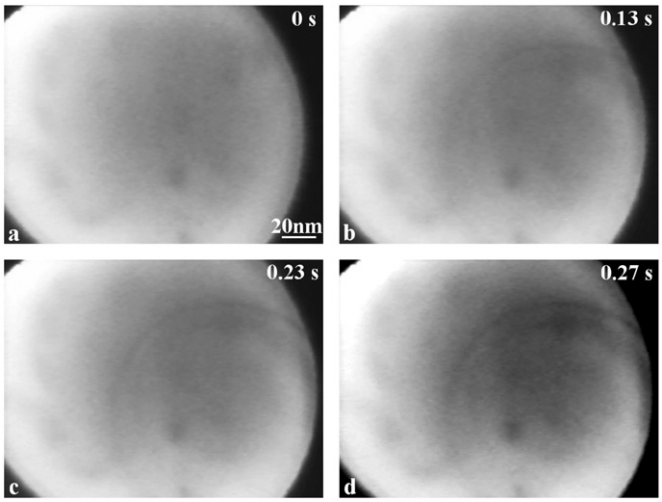


**Fig. 6.** EFTEM, 15 eV energy losses, a 6 eV window. The video frames acquired after 0.0 s (a), 0.13 s (b), 0.23 s (c) and 0.27 s (d). The solid Al nanoparticle rotates in the liquid alloy due to a torque induced by electron-beam irradiation that results in variations of the particle visibility. Thickness fringes demonstrate that the solid nanoparticle is crystalline.

In line with our results, numerical calculations of the momentum transferred to particles in vacuum by a passing 200 keV electron as a function of the distance from the electron trajectory to the center of the particle and its size as well as more detailed analysis including higher-multipole moments [16,33] indicate that focused electron beams are able to trap metal and dielectric spherical particles of up to 500 nm in size. Moreover, the calculated time-average forces and the momentum transfer appear to be comparable in magnitude to laser-induced forces and the momentum transferred by refracted light in conventional optical tweezers and stretchers (see Figs. 2 and 3 in [16]). This also illustrates their common origin as *polarizability-dependent refracted forces induced by the applied electromagnetic field* [2,3,8].

The fields of VPs and SPs generated inside a molten alloy submicron sphere, at solid–liquid interfaces, in a solid Al particle, and in an oxide shell discussed in Section 3.1, in turn affect the distribution of induced trapping force in the material. So, calculations of trapping potential and force distributions for a metal nanostructure located in the vicinity of the trapping focus [11] predict that even for an excitation wavelength that is tuned far from the plasmonic resonance of the nanostructure, the presence of the latter should significantly alter the trap potential. One can expect that the superposition of a trapping non-resonant Gaussian field with an additional plane-wave illumination tuned to the particular plasmonic resonance could give an effective handle to modify the trapping potential and, in principle, make imaging of levitated unsupported nano-objects possible [2,3]. A CdSe nanocrystal trapped in a 3D Coulomb potential well and levitating over a carbon film in a TEM has been reported recently [34]. The polarization and intensity of the resonant illumination may allow modification of the equilibrium position of the trapping potential, thus providing additional means to steer, align and manipulate trapped particles with much higher precision and sensitivity. Further investigation of electron-beam trapping with a single atom level selectivity and sub-70 pm spatial resolution provided by modern aberration-corrected (S)TEAM instruments [35] is likely to facilitate real-time manipulation of clusters, (self-) assembling, separation and sorting of nanoparticles, small clusters and atoms at atomically flat surfaces and in oscillating electro-magnetic fields and coupling with laser optical tweezers. Particularly, holographic trapping coupled with electron tweezers could offer unique opportunities for exerting unlimited variations of torques and forces on several particles of arbitrary shape.

*In situ* experiments using environmental (S)TEM and environmental or "wet" SEM would be useful to prove the feasibility of electron tweezers for 3D-trapping of colloidal metal and dielectric particles in aqueous and non-aqueous media and manipulating nanoparticles in shaped confined volumes such as nanotubes, porous media and complex networks of connected channels. A fast and precise control of all thermal and non-thermal displacements of the particles remains indispensable and efforts still need to be undertaken to improve electron tweezers and to realize new ideas (coupling with laser light, trapping of small clusters, atoms and shaped particles by a tip, on atomic flat surfaces, in channels, and assembling sequencing).

For particles sitting on a substrate, trapping and steering can be potentially made easier (a) on atomically flat surfaces with no strong interactions between the particle and the substrate that sufficiently reduces surface adhesion and friction; (b) on particles levitating over the surface [34] and/or (c) in thin low-viscosity liquid layers deposited on solid substrates following evaporation of solvents. Similar to conventional optical trapping, the electromagnetic gradient force induced by fast refracted electrons should dominate over adhesion and friction forces to make manipulation of particles possible. In this case the optimal heating regime possibly coupled with other types of suitable processing such as laser shock waves or ultrasonic pulse could assist in detaching the particle from the substrate in order to induce the particle's controlled motion over the surface. At the same time, however, disruptive effects of Brownian fluctuations should be avoided.

For probing of even smaller structures and samples relevant in (bio-) nanotechnology, novel probes have to be found, enabling a stronger interaction with electrons, ions and light, resulting in more stable traps and more precise position tracking for exciting applications in nanofabrication [8]. VP, SP and exciton resonances need to be exploited using metallic, semiconductor or dielectric materials with the smallest electron probes.

## 4. Conclusions

In this work, we have demonstrated touchless trapping and steering of solid Al nanoparticles contained inside opaque submicron-sized molten Al–Si alloy spheres by a single electron beam. For this purpose, we utilized the focused electron beam both for fine temperature control during generation, trapping, steering and real-time imaging of 20–300 nm diameter solid Al particles inside molten Al–Si eutectic alloy spheres using the first plasmon at 15 eV. This approach enabled us to investigate *in situ* melting and crystallization phenomena within individual binary alloy particles and to monitor nanoscale transformations of their internal structure, temperature shifts of plasmon peaks, local electronic and optical properties by EFTEM/VEELS. Depending on the available internal volume of the molten sphere, 40–200 nm diameter metal nanoparticles could be easily transferred across distances of 40–100 nm at speeds of 20–40 nm/s in chosen directions by beam shifting, tilting and/or shifting the microscope stage. For particles below 20 nm in size, we observed at 1/30 s time resolution enhanced vibrations of the solid–liquid interface due to instabilities near the critical threshold just before melting. We also observed changes in orientation caused by rotation of the solid Al nanoparticle inside the partially molten submicron particle as a result of angular momentum transfer under electron-beam irradiation. Experimental results indicate that thermally assisted "electron tweezers" potentially can be utilized for manipulation and processing of individual nano-objects and fabrication of assembled nano-devices. The new technique can be superior or complement conventional optical tweezers in the following important aspects:

(a) *Spatial resolution and selectivity*. Modern aberration-corrected (S)TEAM instruments offer sub-70 pm spatial resolution and up to a single atom level selectivity using ultra-fine electron probes, and these quantities are three order of magnitude better than light microscopy techniques employed in conventional optical tweezers.

(b) *Outstanding technical capabilities and flexibility*. High-resolution electron imaging, diffraction and spectroscopy capabilities in various modes not available in conventional optical tweezers, can likely facilitate real-time manipulation of small particles, clusters and even single atoms coupled with comprehensive nanoscale characterization of related structures. The current-state-of-the-art enables one to perform *in situ* experiments in an environmental (S)TEM and environmental or "wet" S(T)EM. The latter would be useful to prove the feasibility of electron tweezers for 3D-trapping of colloidal metal and dielectric particles in aqueous and non-aqueous media and manipulating nanoparticles at surfaces and in shaped confined volumes such as nanotubes, porous media and complex networks of connected channels.

(c) *Non-zero momentum transfer and plasmon resonance tuning*. Electron beam-induced plasmon resonances are not limited to zero-momentum transfer as in conventional optical tweezers.

The fields of VPs and SPs generated inside a molten alloy submicron sphere, at solid–liquid interfaces, in a solid Al particle, and in an oxide shell can affect the distribution of induced trapping force in the material. The superposition of a trapping non-resonant Gaussian field with an additional plane-wave illumination tuned to the particular plasmonic resonance could give an effective handle to modify the trapping potential. The polarization and intensity of the resonant illumination may allow modification of the equilibrium position of the trapping potential, thus providing additional means to steer, align and manipulate trapped particles with high precision and sensitivity.

(d) *Levitation of unsupported nano-objects*. Electron tweezers are suitable to make possible imaging of levitated unsupported nano-objects as it was recently reported for a nanoparticle trapped in a 3D Coulomb potential well and levitating over a carbon film in a TEM.

(e) *Coupling with laser optical tweezers*. Holographic trapping coupled with electron tweezers could offer unique opportunities for exerting unlimited variations of torques and forces on several particles of arbitrary shape.

## Acknowledgements

This research was supported by the US Department of Energy (Grant no. DE-FG02-01ER45918) and by National Institute of Standards and Technology (Contracts SB134110SE0579 and SB134111SE0814). The authors are grateful to Mr. T. Yokota (JFE Steel Corp., Japan) for his help in this research and to Prof. F.J.G. de Abajo (Instituto de Optica-CSIC, Madrid, Spain) for useful discussions. Critical reading of this manuscript by Drs. J. Bonevich and D. Josell, NIST is gratefully acknowledged.

## References

[1] A. Ashkin, Physical Review Letters 24 (1970) 156–159.
[2] A. Ashkin, IEEE Journal 8 (2000) 841–856.
[3] A. Ashkin, Proceedings of the National Academy of Sciences USA 94 (1997) 4853–4860.
[4] A. Ashkin, J.M. Dziedzic, Science 235 (1987) 1517–1520.
[5] P.M. Hansen, V.K. Bhatia, N. Harrit, L. Oddershede, Nano Letters 5 (2005) 1937–1942.
[6] A. Rohrbach, E.H.K. Stelzer, Optical Imaging and Microscopy, in: P. Torok, F.-J. Kao (Eds.), Springer Series in Optical Sciences, 87, Springer-Verlag, Berlin, 2007, pp. 455–489.
[7] M. Pelton, M. Liu, H.Y. Kim, G. Smith, P. Guyot-Sionnest, N.F. Scherer, Optics Letters 31 (2006) 2075–2077.
[8] D.G. Grier, Nature 424 (2003) 810–816.
[9] D.G. Grier, Y. Roichman, Applied Optics 45 (2006) 880–887.
[10] M. Righini, A.S. Zelenina, C. Girard, R. Quidant, Nature Physics 3 (2007) 477–480.
[11] F.J. Garcıa de Abajo, T. Brixner, W. Pfeiffer, Journal of Physics B 40 (2007) S249–S258.
[12] T. Yokota, J.M. Howe, W.A. Jesser, M. Murayama, Journal of Applied Physics 95 (2004) 5756–5761.
[13] J.M. Howe, T. Yokota, M. Murayama, W.A. Jesser, Journal of Electron Microscopy 53 (2004) 107–114.
[14] V.P. Oleshko, J.M. Howe, Microscopy and Microanalysis 10 (Suppl. 2) (2004) 350–351.
[15] V.P. Oleshko, J.M. Howe, Microscopy and Microanalysis 11 (Suppl. 2) (2005) 1512–1513.
[16] F.J.G. de Abajo, Physical Reveiw B 70 (2004) 115422-1-6.
[17] A. Reyes-Coronado, R.G. Barrera, P.E. Batson, P.M. Echenique, A. Rivacoba, J. Aizpurua, Physical Reveiw B 82 (2010) 235429-1-19.
[18] R. Erni, M.D. Rossell, Ch. Kisielowski, U. Dahmen, Physical Review Letters 102 (2009) 096101–1-4.
[19] V.P. Oleshko, J.M. Howe, Journal of Applied Physics 101 (2007) 054308–1-5.
[20] V.P. Oleshko, P.A. Crozier, R.D. Cantrell, A.D. Westwood, Journal of Electron Microscopy 51 (Suppl) (2002) S27–S39.
[21] J.G. Lee, H. Mori, H. Yasuda, Physical Reveiw B 66 (2002) 012105–1-4.
[22] J.L. Murray, A.J. McAlister, Bulletin of Alloy Phase Diagrams 5 (1984) 74–84.
[23] G.A. Storaska, J.M. Howe, Materials Science and Engineering A 368 (2004) 183–190.
[24] H. Raether, in Springer Tracts in Modern Physics, Springer-Verlag, Berlin, 1965 v. 38, pp. 85-157.
[25] S. Tsukimoto, S. Arai, M. Konno, T. Kamino, K. Sasaki, H. Saka, Journal of Microscopy 203 (2001) 17–21.
[26] F.J.G. de Abajo, Reviews of Modern Physics 82 (2010) 209–275.
[27] R. Smith, E. Shiles, M. Inokuti, in: Handbook of Optical Constants of Solids, Academic Press, London, 1998, vol. 1, pp. 369–405.
[28] R. Agayan, F. Gittes, R. Kopelman, C.F. Schmidt, Applied Optics 41 (2002) 2318–2327.
[29] J.D. Jackson, Classical Electrodynamics, Wiley, New York, 1975, pp. 186, 239.
[30] H. Raether, Excitations of Plasmons and Interband Transitions by Electrons, Springer-Verlag, Berlin, 1980, pp. 10–11.
[31] L.W. Hobbs, in: J.J. Hren, J.L. Goldstein, D.C. Joy (Eds.), Introduction to Analytical Electron Microscopy, Plenum, New York, 1977, pp. 437–480.
[32] F.J.G. de Abajo, private communication.
[33] F.J.G. de Abajo, Journal of Quantitative Spectroscopy 89 (2004) 3–9.
[34] S.-Y. Xu, W.-Q. Sun, M. Zhang, J. Xu, L.-M. Peng, Nanoscale 2 (2010) 248–253.
[35] P.E. Batson, Microscopy and Microanalysis 14 (2008) 89–97.